

# Rotating nonlinear states in trapped binary Bose-Einstein condensates under the action of the spin-orbit coupling

Hidetsugu Sakaguchi<sup>1</sup> and Boris A. Malomed<sup>2,3,a</sup>

<sup>1</sup>*Interdisciplinary Graduate School of Engineering Sciences,  
Kyushu University, Kasuga, Fukuoka, 816-8580, Japan*

<sup>2</sup>*Department of Physical Electronics, School of Electrical Engineering, Faculty of Engineering,  
and Center for Light-Matter Interaction, Tel Aviv University, Tel Aviv, 69978, Israel*

<sup>3</sup>*Instituto de Alta Investigación, Universidad de Tarapacá, Casilla 7D, Arica, Chile*

We report results of systematic analysis of confined steadily rotating patterns in the two-component BEC including the spin-orbit coupling (SOC) of the Rashba type, which acts in the interplay with the attractive or repulsive intra-component and inter-component nonlinear interactions and confining potential. The analysis is based on the system of the Gross-Pitaevskii equations (GPEs) written in the rotating coordinates. The resulting GPE system includes effective Zeeman splitting. In the case of the attractive nonlinearity, the analysis, performed by means of the imaginary-time simulations, produces deformation of the known two-dimensional SOC solitons (semi-vortices and mixed-modes). Essentially novel findings are reported in the case of the repulsive nonlinearity. They demonstrate patterns arranged as chains of unitary vortices which, at smaller values of the rotation velocity  $\Omega$ , assume the straight (single-string) form. At larger  $\Omega$ , the straight chains become unstable, being spontaneously replaced by a trilete star-shaped array of vortices. At still large values of  $\Omega$ , the trilete pattern rebuilds itself into a star-shaped one formed of five and, then, seven strings. The transitions between the different patterns are accounted for by comparison of their energy. It is shown that the straight chains of vortices, which form the star-shaped structures, are aligned with boundaries between domains populated by plane waves with different wave vectors. A transition from an axisymmetric higher-order (multiple) vortex state to the trilete pattern is investigated too.

## I. INTRODUCTION

Bose-Einstein condensates (BECs) in atomic gases offer a versatile platform for the creation of various nonlinear modes in quantum matter. These possibilities were realized experimentally for vortices [1–4], effectively one-dimensional (1D) matter-wave solitons [5–7], including gap solitons [8], weakly unstable (hence experimentally observable) solitons of the Townes type in two dimensions (2D) [9, 10], multidimensional “quantum droplets” [11–14] in binary BEC, whose stability is provided by effects of quantum fluctuations [15, 16], etc.

The usual cubic (mean-field) self-attractive nonlinearity readily predicts matter-wave solitons in the 2D and 3D free space, but they are made unstable by the critical or supercritical collapse (in 2D or 3D, respectively) [18–20]. Therefore, many works aimed to elaborate conditions for the creation of *stable* 2D and 3D matter-wave solitons. An especially challenging problem is the stabilization of multidimensional solitons with embedded vorticity, which, in the framework of basic settings, are subject to a still stronger splitting instability [20].

A promising possibility for the creation of stable 2D [21–31] and 3D [32] solitons is offered by the binary BEC with the self- and cross-attractive cubic interactions between its two components, which are, in addition, linearly mixed, through their spatial gradients, by the spin-orbit coupling (SOC). In the experiment, SOC is induced by a properly designed set of laser beams illuminating the condensate [33–35]. The possibility to stabilize multidimensional matter-wave solitons by SOC is upheld by the fact that SOC has been theoretically predicted [36] and experimentally realized [37] in 2D, while the attractive sign of the nonlinearity may be provided by the Feshbach resonance [38–41]. Depending on the relative strength of the self- and cross-component cubic attraction, the SOC systems give rise to absolutely stable 2D [21, 22] and metastable 3D [32] solitons of two types: semi-vortices (SVs) and mixed modes (MMs). Under the action of SOC, stable SVs are built as compounds with zero vorticity in one component, and vorticity 1 in the other [21, 32], or their mirror images, with vorticities  $-1$  and  $0$  in the two components. The MM is produced, approximately, as a combination of the SV and its mirror image.

In addition to the lowest-order (fundamental) SVs and MMs, the respective system of coupled 2D Gross-Pitaevskii equations (GPEs) admits solutions for *excited states* of SVs and MMs, with equal vorticities added to both components. In the case of the completely attractive nonlinear interactions, all the excited states are unstable [21]. They may be stabilized in the system with opposite signs of the self-interaction in the two components [31].

---

<sup>a</sup> The corresponding author: malomed@tauex.tau.ac.il

Another natural generalization of nonlinear SOC modes is to consider them in the rotating form, with the centrifugal force balanced by an axisymmetric trapping potential. This possibility was addressed in Refs [42, 43] (without a relation to the SV and MM solitons) and [23] (the model introduced in the latter work included the coupled GPEs in the form which implied that the SOC-inducing set of laser beams was rotating, which is not quite a realistic setup for the experiment). Here, we aim to obtain various forms of stable rotating matter-wave modes, which are related, in particular, to the SVs and MMs in the usual (non-rotating) situation (assuming that the modes are set in rotation, while the underlying SOC-inducing optical beams remain quiescent). To this end, the relevant system of GPEs in the rotating reference frame is introduced in Section II. The appropriate transformation casts the system in a form which is somewhat similar to that derived in Ref. [23], with an essential difference that the transformed equations include effective Zeeman-splitting (ZS) terms, which are induced by the rotation of BEC with respect to the SOC-inducing optical framework. It is known that ZS may produce strong effects in SOC systems [43–45].

Stable solutions, which are stationary in the rotating coordinates, are obtained, for the attractive and repulsive signs of the nonlinear interactions, in Sections III and IV, respectively. In the former case, numerical analysis, performed by means of the imaginary-time simulations [46, 47], produces, essentially, SV and MM solitons deformed by the rotation. In the latter case (the repulsive interactions), the numerical results demonstrate, first, formation of single- and multi-layer circular vortex lattices, which resemble the patterns previously reported in Refs. [23, 42, 43]. Most remarkable are completely novel patterns which are revealed, in the case of the repulsive nonlinearity, by the systematic numerical analysis, following the increase of the main control parameter, *viz.*, the rotation angular velocity,  $\Omega$ . At first, it leads to generation of multiple-vortex arrays which line up along a straight string. Further increase of  $\Omega$  destabilizes the rectilinear array of vortices, replacing it by a star composed of three and, at still large values of  $\Omega$ , of five and seven strings. The inferences produced by this work are formulated in concluding Section V.

## II. THE MODEL

The well-known 2D model of SOC of the Rashba type with strength  $\lambda > 0$  is based on the following system of GPEs for wave functions  $\phi_{\pm}(X, Y, t)$  of the two components of the binary BEC, written in the scaled form [21],

$$\begin{aligned} i\frac{\partial\phi_+}{\partial t} &= -\frac{1}{2}\nabla^2\phi_+ + g\left(|\phi_+|^2 + \gamma|\phi_-|^2\right)\phi_+ + U(r)\phi_+ + \lambda\left(\frac{\partial}{\partial X} - i\frac{\partial}{\partial Y}\right)\phi_-, \\ i\frac{\partial\phi_-}{\partial t} &= -\frac{1}{2}\nabla^2\phi_- + g\left(|\phi_-|^2 + \gamma|\phi_+|^2\right)\phi_- + U(r)\phi_- + \lambda\left(-\frac{\partial}{\partial X} + i\frac{\partial}{\partial Y}\right)\phi_+, \end{aligned} \quad (1)$$

where  $(X, Y)$ , with  $\nabla^2 = \partial^2/\partial X^2 + \partial^2/\partial Y^2$ , are the Cartesian coordinates in the laboratory reference frame,  $g$  is the overall strength of the nonlinear interactions,  $g < 0$  and  $g > 0$  corresponding to the attraction and repulsion, respectively,  $\gamma \geq 0$  is the relative strength of the inter-component interaction with respect to the self-interaction, and  $U(r)$  is the trapping potential, which we adopt, as usual, in the harmonic-oscillator form,

$$U(r) = (1/8)(x^2 + y^2) \quad (2)$$

(the coefficient in this expression is fixed by means of scaling).

Coordinates  $(x, y)$  in the reference frame rotating with angular velocity  $\Omega$  are defined as usual,

$$\begin{aligned} x &= X \cos(\Omega t) + Y \sin(\Omega t), \\ y &= Y \cos(\Omega t) - X \sin(\Omega t), \end{aligned} \quad (3)$$

The GPE system (1), transformed into the rotating coordinates (3), takes the following explicitly time-dependent form:

$$\begin{aligned} i\frac{\partial\phi_+}{\partial t} &= -\frac{1}{2}\nabla^2\phi_+ + g\left(|\phi_+|^2 + \gamma|\phi_-|^2\right)\phi_+ + U(\mathbf{r})\phi_+ - \Omega\hat{L}_z\phi_+ + \lambda e^{-i\Omega t}\left(\frac{\partial}{\partial x} - i\frac{\partial}{\partial y}\right)\phi_-, \\ i\frac{\partial\phi_-}{\partial t} &= -\frac{1}{2}\nabla^2\phi_- + g\left(|\phi_-|^2 + \gamma|\phi_+|^2\right)\phi_- + U(\mathbf{r})\phi_- - \Omega\hat{L}_z\phi_- + \lambda e^{i\Omega t}\left(-\frac{\partial}{\partial x} + i\frac{\partial}{\partial y}\right)\phi_+, \end{aligned} \quad (4)$$

where  $\hat{L}_z = i(y\partial_x - x\partial_y)$  is the angular-momentum operator, and the Laplacian is now written as  $\nabla^2 = \partial^2/\partial x^2 + \partial^2/\partial y^2$ . The time dependence in Eqs. (4) may be removed by the substitution

$$\phi_{\pm} \equiv \psi_{\pm} \exp\left(\mp i\frac{\Omega}{2}t\right), \quad (5)$$

which transforms the system into a form similar to the one which was introduced in Ref. [23], but with additional terms which are tantamount to the effective ZS, with strength  $\Omega/2$ :

$$\begin{aligned} i\frac{\partial\psi_+}{\partial t} &= -\frac{1}{2}\nabla_+^2\psi_+ + g\left(|\psi_+|^2 + \gamma|\psi_-|^2\right)\psi_+ + U(\mathbf{r})\psi_+ - \Omega\hat{L}_z\psi_+ + \lambda\left(\frac{\partial}{\partial x} - i\frac{\partial}{\partial y}\right)\psi_- - \frac{\Omega}{2}\psi_+, \\ i\frac{\partial\psi_-}{\partial t} &= -\frac{1}{2}\nabla_-^2\psi_- + g\left(|\psi_-|^2 + \gamma|\psi_+|^2\right)\psi_- + U(\mathbf{r})\psi_- - \Omega\hat{L}_z\psi_- + \lambda\left(-\frac{\partial}{\partial x} + i\frac{\partial}{\partial y}\right)\psi_+ + \frac{\Omega}{2}\psi_-. \end{aligned} \quad (6)$$

The ZS makes component  $\psi_+$  energetically preferable in comparison with  $\psi_-$ .

Various stationary states reported below were produced by imaginary-time simulations of Eq. (6). The initial condition

$$(\psi_+)_0 = 0.5 \exp(-x^2 - y^2), \quad (\psi_-)_0 = 0.3 \exp(-x^2 - y^2) \quad (7)$$

was used for the simulations in most cases, unless indicated otherwise.

The system of coupled GPEs (6) has three usual dynamical invariants, *viz.*, the total norm (proportional to the number of atoms in the condensate),

$$N = \iint \left(|\psi_+|^2 + |\psi_-|^2\right) dx dy, \quad (8)$$

total angular momentum,

$$M = \iint \left(\psi_+^* \hat{L}_z \psi_+ + \psi_-^* \hat{L}_z \psi_-\right) dx dy + \Omega N, \quad (9)$$

and energy

$$\begin{aligned} E &= \iint \sum_{\pm} \left\{ \frac{1}{2} |\nabla \psi_{\pm}|^2 + \frac{g}{2} |\psi_{\pm}|^4 + U(r) |\psi_{\pm}|^2 \right. \\ &\quad \left. \lambda \left[ \psi_+^* \left( \frac{\partial \psi_-}{\partial x} - i \frac{\partial \psi_-}{\partial y} \right) + \psi_-^* \left( -\frac{\partial \psi_+}{\partial x} - i \frac{\partial \psi_+}{\partial y} \right) \right] \right. \\ &\quad \left. - \Omega \left[ i \sum_{\pm} \psi_{\pm}^* \left( -x \frac{\partial}{\partial y} + y \frac{\partial}{\partial x} \right) \psi_{\pm} + \frac{|\psi_+|^2 - |\psi_-|^2}{2} \right] \right\} dx dy, \end{aligned} \quad (10)$$

where \* stands for the complex conjugate. Note that  $M$  is conserved in spite of the formally anisotropic form of the angular-momentum and SOC operators in Eq. (6), cf. Refs. [27, 31]. Term  $\Omega N$  in Eq. (9) is the contribution to the angular momentum from the overall rotation of the matter-wave state with respect to the laboratory coordinates (in fact, this term is not essential, as  $N$  is conserved separately).

### III. NUMERICAL RESULTS IN THE CASE OF ATTRACTIVE INTERACTIONS

In this section, we consider the case of  $g < 0$ , which corresponds to the attractive nonlinearity in Eq. (6). The analysis starts from finding linear eigenstates corresponding to  $g = 0$  and  $\Omega > 0$ .

Figure 1 shows stable vortex state produced by the numerical solution for a set of increasing values of the self-attraction strength, *viz.*,  $g = -0.01$  (a),  $g = -0.1$  (b), and  $g = -0.5$  (c), fixing other parameters and the norm as  $\lambda = 2$ ,  $\gamma = 0$ ,  $\Omega = 0.3$ , and  $N = 4$ . The attractive interaction makes the wave function spontaneously localized in the azimuthal direction, producing a crescent-like soliton in Fig. 1(b) and a still more compact one in Fig. 1(c). The transition from the nearly axisymmetric state to the one self-trapped in the azimuthal direction is similar to that reported in Ref. [49]

SV states in the attractive nonrotating system ( $\Omega = 0$ ) are stable at  $\gamma < 1$  (i.e., if the self-attraction is stronger than the inter-component attraction) [21]. These states persist in the rotating system with  $\Omega > 0$ . We study their evolution, following the variation of parameter  $\gamma$ , as it is critically important for the SVs' stability. Figure 2(a) shows profiles of  $|\psi_+(x, y)|$  and  $|\psi_-(x, y)|$  (solid and dashed lines, respectively) in the cross section  $y = 0$  at  $\gamma = 1.5, 1.4, 1.3, 1.2, 1.1$ , and 1, fixing  $g = -1$ ,  $\Omega = 0.35$ ,  $\lambda = 0.5$ , and  $N = 3$ . Stable SVs are found at  $\gamma = 1$  and 1.1, satisfying their familiar property of vanishing the average value of  $x$  [21], i.e.,

$$\langle x \rangle = \iint x |\psi_+|^2 dx dy / \iint |\psi_+|^2 dx dy = 0. \quad (11)$$

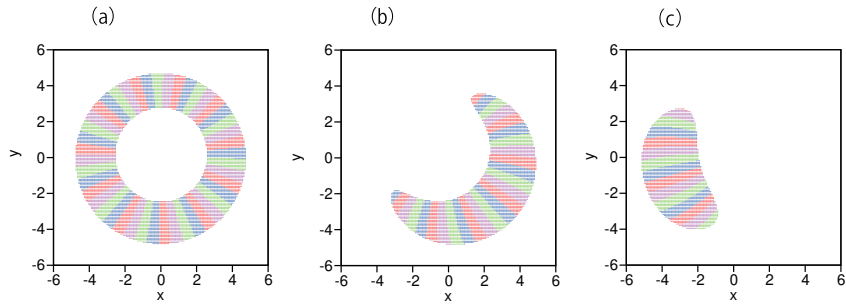


FIG. 1. (a) The numerically found vortex state for  $g = -0.01$ . (b) The crescent-like state obtained for  $g = -0.1$ . (c) The semi-vortex soliton obtained for  $g = -0.5$ . The other parameters are  $\gamma = 0$ ,  $\Omega = 0.3$ ,  $\lambda = 2$ , and  $N = 4$ . Here and below (see Figs. 4-8 and 10-13) the area with  $|\psi_+| > 0.08$  is plotted by different colors indicating regions with  $\text{Re}\psi_+ > 0$  and  $\text{Im}\psi_+ > 0$  (green);  $\text{Re}\psi_+ < 0$  and  $\text{Im}\psi_+ > 0$  (blue);  $\text{Re}\psi_+ < 0$  and  $\text{Im}\psi_+ < 0$  (red);  $\text{Re}\psi_+ > 0$  and  $\text{Im}\psi_+ < 0$  (magenta). This color coding makes it possible to display both amplitude and phase profiles of  $\psi_+$  in the single figure.

In this vein, Fig. 2(b) shows  $-\langle x \rangle$  as a function of  $\gamma$  for  $g = -1$ ,  $\Omega = 0.35$ ,  $\lambda = 0.5$ , and  $N = 3$ . The SV transition to an unstable states with  $\langle x \rangle \neq 0$  occurs  $\gamma = 1.16$  (however, the instability does not transform the SVs into MMs).

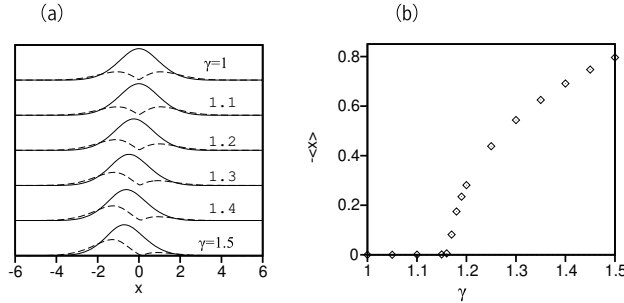


FIG. 2. (a) Profiles of  $|\psi_+(x, y)|$  and  $|\psi_-(x, y)|$  (solid and dashed lines) in the cross section  $y = 0$  for  $\gamma = 1.5, 1.4, 1.3, 1.2, 1.1$ , and  $1$ , fixing  $g = -1$ ,  $\Omega = 0.35$ ,  $\lambda = 0.5$ , and  $N = 3$ . (b) The average value  $-\langle x \rangle$  (see Eq. (11)) vs.  $\gamma$  for  $g = 1$ ,  $\Omega = 0.35$ ,  $\lambda = 0.5$ , and  $N = 3$ .

Further, Fig. 3(a) shows the profiles of  $|\psi_+(x)|$  and  $|\psi_-(x)|$  (the solid and dashed lines, respectively) in the cross section  $y = 0$  for  $\Omega = 0.17, 0.2$ , and  $0.23$ , fixing

$$g = -1, \gamma = 0, \lambda = 2, N = 4. \quad (12)$$

The usual stable SV state exists at  $\Omega = 0.17$ , while the peak position of  $|\psi(x)|$  shifts to the right at  $\Omega = 0.2$  and  $0.23$ . For the same parameter set (12), Figure 3(b) shows the  $x$  coordinate of the soliton's center of mass.

$$X = \frac{\int \int (|\psi_+|^2 + |\psi_-|^2) x dx dy}{\int \int (|\psi_+|^2 + |\psi_-|^2) dx dy}, \quad (13)$$

with respect to the fact that  $(|\psi_+|^2 + |\psi_-|^2)$  is the total density of the condensate (cf. Eq. (8)). The center of mass deviates from  $x = 0$  at  $\Omega \geq 0.188$ , featuring a weak hysteresis revealed by the variation of  $\Omega$ . Figure 3(c) shows the  $x$  coordinate of the soliton's center of mass for  $g = -1$ ,  $\gamma = 0$ ,  $\lambda = 1$ , and  $N = 4$ , which continuously deviates from  $x = 0$  in this case.

Figures 4(a) and (b) show wave patterns of the MM type of  $\psi_-(x, y)$  at (a)  $\Omega = 0$  and (b)  $\Omega = 0.36$  for  $g = -1$ ,  $\gamma = 2$ ,  $\lambda = 2$ , and  $N = 1$ . Figure 4(a) produces a stable MM state at  $\Omega = 0$ . In this case, the center of mass of the MM state is located at the origin. The MM state shown in Fig. 4(a) for  $\Omega = 0$  features a vortex centered at  $x \simeq 0.66$  and  $y = 0$ . As  $\Omega$  increases, the center of mass shifts to the left, and soliton-like state, similar to the one observed in Fig. 1(c), appears in Fig. 4(b) at  $\Omega = 0.36$ . For large  $\Omega$ , the center of mass of the localized state is driven off the origin by the centrifugal force. Figure 4(c) shows the center-of-mass coordinates of the two components,

$$\langle x_{\pm} \rangle = \frac{\int \int x |\psi_{\pm}|^2 dx dy}{\int \int |\psi_{\pm}|^2 dx dy}, \quad (14)$$

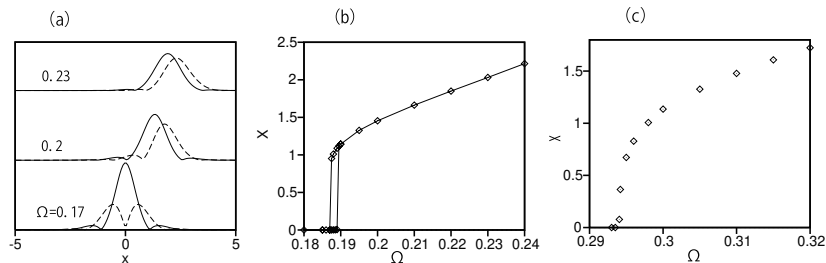


FIG. 3. (a) Profiles of  $|\psi_+(x)|$  and  $|\psi_-(x)|$  (solid and dashed lines) in the cross section  $y = 0$  at  $\Omega = 0.17, 0.2$ , and  $0.23$  for  $g = -1$ ,  $\gamma = 0$ ,  $\lambda = 2$ , and  $N = 4$ . (b) The  $x$  coordinate of the center of mass, defined as per Eq. (13) for  $g = -1$ ,  $\gamma = 0$ ,  $\lambda = 2$ , and  $N = 4$ . (c) The  $x$  coordinate of the center of mass, defined as per Eq. (13) for  $g = -1$ ,  $\gamma = 0$ ,  $\lambda = 1$ , and  $N = 4$ .

(the solid and dashed lines; cf. Eq. (13)) as a function of  $\Omega$ . At  $\Omega = 0$ ,  $\langle x_+ \rangle = 0.156$  and  $\langle x_- \rangle = -0.156$ , hence the center of the mass of the entire MM state is located at  $x = 0$ , as said above. As  $\Omega$  increases,  $\langle x_+ \rangle$  decreases monotonously, while  $\langle x_- \rangle$  features a small peak at  $\Omega \simeq 0.05$  and then decreases.

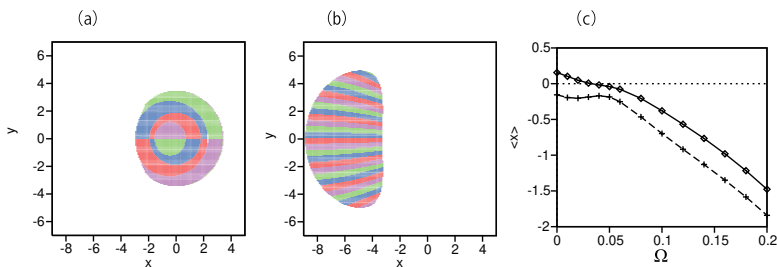


FIG. 4. Patterns of  $|\psi_-(x,y)|$  for the MM states at (a)  $\Omega = 0$  and (b)  $\Omega = 0.36$ , for  $g = -1$ ,  $\gamma = 2$ ,  $\lambda = 2$ , and  $N = 1$ . (c) Coordinates of the center of mass (14) as a function of  $\Omega$ .

#### IV. NUMERICAL RESULTS IN THE CASE OF REPULSIVE INTERACTIONS

In this section, we address the system with the repulsive nonlinearity,  $g > 0$ . First, we address the transformation of the vortex patterns following the variation of the nonlinearity strength,  $g$ . Figure 5(a) shows a stable axisymmetric higher-order vortex state with the vortex number (topological charge)  $VN = 11$  for  $g = 1$ ,  $\lambda = 2$ ,  $\gamma = 0$ ,  $\Omega = 0.3$ , and  $N = 4$ . Figure 5(b) shows a circular vortex lattice, built of 7 unitary vortices, which surrounds the higher-order vortex with  $VN = 7$  located at the center, for  $g = 10$ ,  $\gamma = 0$ ,  $\lambda = 2$ ,  $\Omega = 0.3$ , and  $N = 4$ . Further, Fig. 5(c) shows a more complex vortex lattice, including the outer and inner layers, built of 8 and 6 unitary vortices, respectively, and the higher-order vortex with  $VN = 5$  located at the center, for  $g = 30$ ,  $\gamma = 0$ ,  $\lambda = 2$ ,  $\Omega = 0.3$ , and  $N = 4$ . The repulsive interaction naturally drives delocalization of the pattern and creation of additional vortices. We categorize the vortex patterns in Figs. 5(b) and (c) as two- and three- layer structures, counting the central higher-order vortex. Actually, the vortex layers appear at domain boundaries separating different areas of the underlying background field. These vortex lattices are similar to ones reported in previously studied models [23, 42, 43] (in particular, the Ref. [23] dealt with a system similar to Eq. (6), but without the effective ZS terms).

At a fixed value of  $g$ , the central vortex with  $VN > 1$  appear following the increase of  $\Omega$ . This is shown in detail in Fig. 6, for the gradual growth of  $\Omega$ :  $0.18 \rightarrow 0.19 \rightarrow 0.20$  (note these values are smaller than  $\Omega = 0.30$ , for which Fig. 5 is plotted). It is observed that two unitary vortices, located near the center in panels (a) and (b), approach each other and merge into the double vortex, with  $VN = 2$ , in panel (c).

Figure 7 shows three patterns of  $\psi_+(x,y)$  at (a)  $\Omega = 0.02$ , (b)  $\Omega = 0.08$ , and (c)  $\Omega = 0.18$  for  $\lambda = 2$ ,  $g = 1$ ,  $\gamma = 0$ , and  $N = 4$ . Figure 7(a) shows an SV state with zero vorticity in the  $\psi_+$  component, Fig. 7(b) shows a state with vorticity  $VN = 1$  in  $\psi_+$ , and in Fig. 7(c) one observes a higher-order vortex with  $VN = 3$  in  $\psi_+$ . In these cases, the vorticity of  $\psi_-$  is larger by 1 than that of  $\psi_+$ , which is the above-mentioned characteristic feature of SV states. For larger  $\Omega$ , a central vortex appears with still larger values of  $VN$ . Additional unitary vortices, which were observed

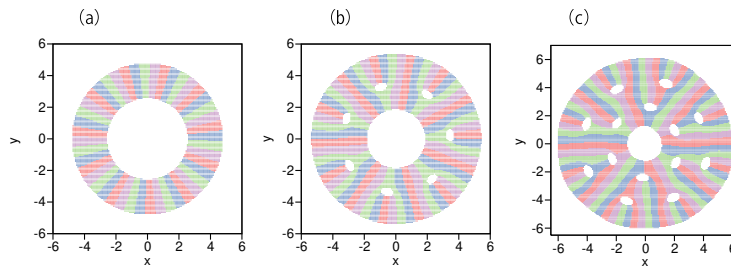


FIG. 5. Vortex patterns produced by the system with the repulsive nonlinearity, *viz.*,  $g = 1$  (a),  $g = 10$  (b), and  $g = 30$  (c). The patterns include higher-order vortices with vortex numbers (topological charges)  $VN = 11$ ,  $7$ , and  $5$  located at the center, which are surrounded by circular layers built of unitary vortices (in panels (b) and (c)). Other parameters and the norm are  $\gamma = 0$ ,  $\Omega = 0.3$ ,  $\lambda = 2$ , and  $N = 4$ .

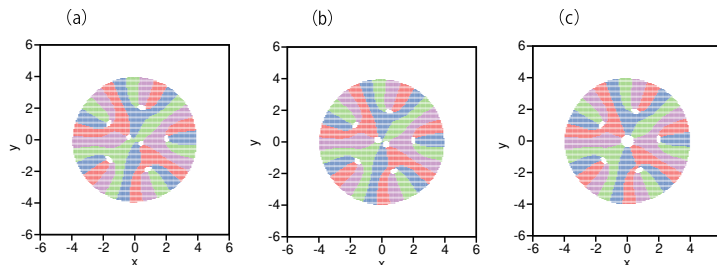


FIG. 6. Vortex patterns at (a)  $\Omega = 0.18$ , (b)  $0.19$ , and (c)  $0.2$  for  $\lambda = 2$ ,  $N = 4$ ,  $g = 10$ , and  $\gamma = 0$ . The central vortex in (c) is a double one, with  $VN = 2$ .

above in Figs. 5(b) and (c), do not appear around the central multiple vortex in the present case.

At large values of  $g$ , the flattening effect of the strong self-repulsion gives rise to a nearly-plane-wave state at  $\Omega = 0$ , in contrast to the SV state observed at  $g = 1$ . Actually, the approximate plane-wave state is observed at  $g \geq 1.5$ , while the other parameters and the norm are fixed as  $\Omega = 0.02$ ,  $\lambda = 2$ ,  $\gamma = 0$ , and  $N = 4$ . We address a transition from the plane wave to structured states as  $\Omega$  varies for fixed  $g = 10$ ,  $\lambda = 2$ ,  $\gamma = 0$ , and  $N = 4$ . First, Fig. 8(a) exhibits the plane-wave state of component  $\psi_+$  at  $\Omega = 0$ , there being no vorticity in this case. Next, Fig. 8(b) shows  $\psi_+$  at  $\Omega = 0.04$ , exhibiting an array of unitary vorticities aligned with the vertical axis,  $x = 0$ . Next, Fig. 8(c) shows the structure of  $\psi_+$  at  $\Omega = 0.13$ .

The vortex arrays, aligned with the single vertical straight line,  $x = 0$ , in Fig. 8(b), or with the three lines,  $x = 0$  and  $y = (\pm 1/\sqrt{3})x$  (at  $x < 0$ ) in Fig. 8(c) (a trilete structure), are arranged by the underlying background, which is composed of plane-wave domains with different wave vectors. In particular, in Fig. 8(b) these are plane waves approximated by  $\exp(iky)$  at  $x > 0$  and  $\exp(-iky)$  at  $x < 0$ . They are separated by the domain wall at  $x = 0$ , to which the vortex array is attached. The trilete state appears at  $\Omega \geq 0.12$ . To illustrate the background structure, Fig. 8(d) shows  $\text{Re}\psi_+$  and  $\text{Im}\psi_+$  (solid green and dashed blue lines, respectively) at cross sections drawn through  $x = -2.49, -1.66, -0.83, 0, 0.83, 1.66$ , and  $2.49$ , for the straight vortex pattern at  $\Omega = 0.09$ . The corresponding peak positions of  $\text{Im}\psi_+$  are located to the right (left) of the peaks of  $\text{Re}\psi_+$  for  $y > 0$  ( $y < 0$ ). The wave pattern shown in Fig. 8(c) is approximated by  $\exp\{-i(\sqrt{3}k/2)x + i(k/2)y\}$  for  $0 < \theta < 2\pi/3$ ,  $\exp(-iky)$  for  $2\pi/3 < \theta < 4\pi/3$ , and  $\exp\{i(\sqrt{3}k/2)x + i(k/2)y\}$  for  $4\pi/3 < \theta < 2\pi$ , where  $\theta$  is the angular coordinate in the  $(x, y)$  plane. Accordingly, the three vortex arrays are aligned with the domain boundaries between the background plane waves, corresponding to  $\theta = 0, 2\pi/3$ , and  $4\pi/3$ . These vortex arrays are similar to the ones reported in Refs. [42, 43].

For the identification of the system's ground state in the case of coexistence of different stationary modes, it is relevant to compute the respective values of energy (10) and thus find a state realizing an energy minimum. Figure 9 produces the results for three states: the plane wave (denoted by  $m = 1$  in Fig. 9); the vortex array aligned with the single boundary between two plane-wave background domains ( $m = 2$ ); and the trilete vortex array attached to boundaries between three background domains ( $m = 3$ ). The energies of these three patterns are exhibited in Fig. 9 as functions of  $\Omega$ . These three species of the patterns were produced by means of the imaginary-time simulations of Eq. (6) with inputs taken, severally, as the plane wave at  $\Omega = 0$ , the single-string vortex array at  $\Omega = 0.04$ , and the trilete array at  $\Omega = 0.16$ . The total energy was computed if a given type of the wave pattern was maintained

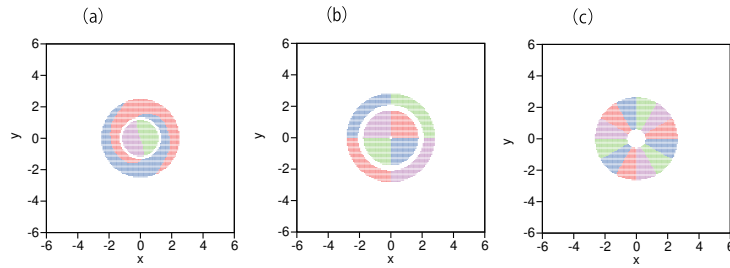


FIG. 7. (a) The  $\psi_+$  component of the SV state for  $\Omega = 0.02$ ,  $\lambda = 2$ ,  $g = 1$ ,  $\gamma = 0$ , and  $N = 4$ . (b) The same, but for  $\Omega = 0.08$  (four times as large as in (a)),  $\lambda = 2$ ,  $g = 1$ ,  $\gamma = 0$ , and  $N = 4$ . In this case, a vortex with  $VN = 1$  is located at the center in the  $\psi_+$  component, and a vortex with  $VN = 2$  is located at the center in  $\psi_-$ . (c) A higher-order vortex with  $VN = 3$  at  $\Omega = 0.18$ .

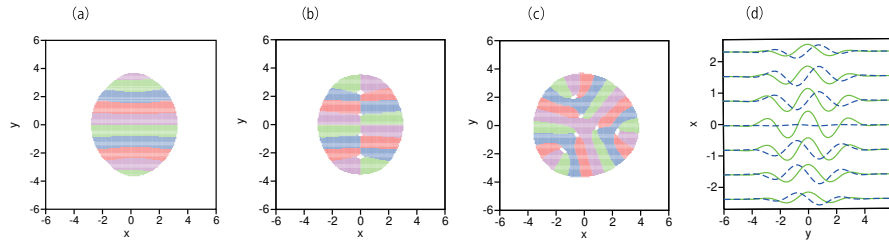


FIG. 8. Patterns of component  $\psi_+$  at (a)  $\Omega = 0$ , (b)  $\Omega = 0.04$ , and (c)  $\Omega = 0.16$  for  $g = 10$ ,  $\gamma = 0$ ,  $\lambda = 2$ , and  $N = 4$ . (d)  $\text{Re}\psi_+$  and  $\text{Im}\psi_+$  (solid green and dashed blue lines, respectively) at cross sections drawn through  $x = -2.49, -1.66, -0.83, 0, 0.83, 1.66,$  and  $2.49$  for  $\Omega = 0.09$ , in the case when the single array of unitary vortices is aligned with the vertical axis,  $x = 0$ .

in the course of the imaginary-time simulations; the data were not recorded if the pattern spontaneously switched in the course of the simulations. Thus, Fig. 9 demonstrates that the plane-wave state, denoted by the chain of rhombuses in the figure, has the lowest energy at  $\Omega < 0.03$ ; the single-string vortex array, which corresponds to the two-domain background, furnishes the lowest energy at  $0.03 \leq \Omega \leq 0.1$ ; and the trilete vortex-array pattern, based on the three-domain background, realizes the lowest energy for  $\Omega > 0.1$ . Thus, we conclude that the background with the increasing number of domains becomes dominant as  $\Omega$  increases.

The trilete pattern built of unitary vortices (similar to the one displayed in Fig. 8(c)) can also develop from the original axisymmetric higher-order vortex state as a result of the increase of the nonlinearity coefficient  $g$ , for fixed values of  $\gamma$ ,  $\lambda$ ,  $\Omega$ , and  $N$ . Figure 10 shows the corresponding patterns at  $g = 0.5$  (a),  $g = 0.65$  (b),  $g = 1$  (c), and  $g = 2$  (d) for  $\gamma = 0$ ,  $\lambda = 4$ ,  $\Omega = 0.1$ , and  $N = 4$ . The stable axisymmetric higher-order vortex state with  $VN = 6$  exists at  $g = 0.5$  and is maintained at  $g = 0.6$ . At  $g = 0.65$ , three unitary vortices are generated at three points with some distance from the origin, while the central vortex keeps  $VN = 6$ . The vortex pattern gets deformed, reducing

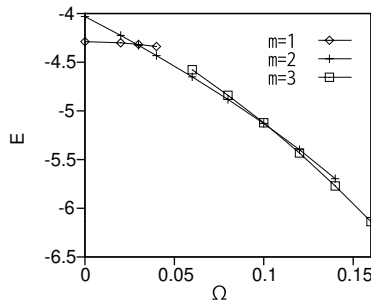


FIG. 9. The total energy  $E$ , defined as per Eq. (10), as a function of the rotation angular velocity  $\Omega$ , for three types of wave patterns, *viz.*, plane waves ( $m = 1$ ), single-string vortex arrays ( $m = 2$ ), and trilete vortex arrays ( $m = 3$ ), for  $\lambda = 2$ ,  $g = 10$ ,  $\gamma = 0$ , and  $N = 4$ .

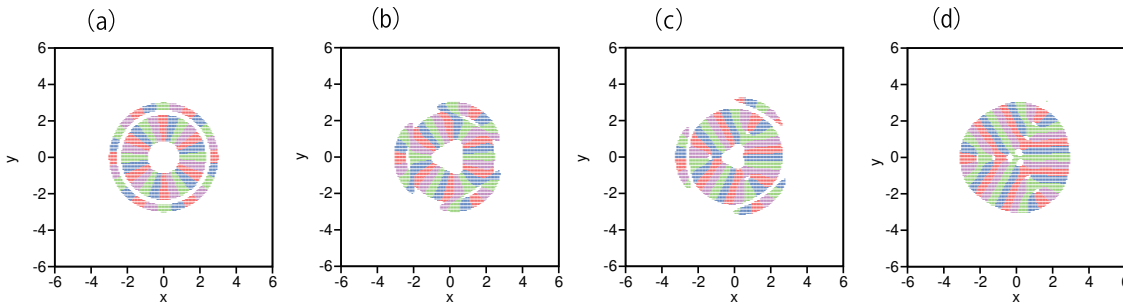


FIG. 10. The transition from the axisymmetric higher-order vortex state to the trilete pattern, following the variation of  $g$ , for  $\gamma = 0$ ,  $\lambda = 4$ ,  $\Omega = 0.1$ , and  $N = 4$ : (a)  $g = 0.5$ , (b)  $g = 0.65$ , (c)  $g = 1$ , and (d)  $g = 2$ .

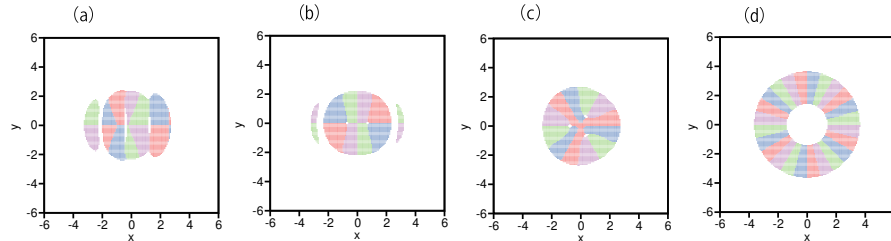


FIG. 11. The wave patterns in the  $\psi_+$  component at  $\Omega = 0$  (a),  $\Omega = 0.08$  (b),  $\Omega = 0.16$  (c), and  $\Omega = 0.24$  (d), for  $g = 1$ ,  $\gamma = 2$ ,  $\lambda = 2$ , and  $N = 4$ .

its rotational isotropy to the three-fold symmetry. At  $g = 1$ , three unitary vortices are released from the origin, and a mixed state appears, including the central higher-order vortex state with the remaining topological charge  $VN = 3$  and the nascent trilete structure. The distance of the satellite vortices from the origin increases with the increase of  $g$ . At  $g = 2$ , the central vortex disappears, and the well-pronounced trilete state arises, as seen in Fig. 10(d).

Next, we vary the rotation angular velocity  $\Omega$  for fixed parameters  $g = 1$ ,  $\gamma = 2$ ,  $\lambda = 2$ , and fixed norm  $N = 4$ . Figure 11 displays the corresponding patterns of component  $\psi_+$  at  $\Omega = 0$  (a),  $\Omega = 0.08$  (b),  $\Omega = 0.16$  (c), and (d)  $\Omega = 0.24$  for  $g = 1$ . An MM state appears at  $\Omega = 0$ . At  $\Omega = 0.08$  two and three unitary vortices are located on the  $x$  axis in the  $\psi_+$  and  $\psi_-$  components, respectively, forming a single-string vortex array. Three vortices are exhibited at  $\Omega = 0.16$  in Fig. 11(c), with four vortices appearing in the respective pattern of component  $\psi_-$  (one of them is located at the center). The latter pattern may be categorized as the nascent trilete state, cf. Fig. 10(c). In Fig. 11(d), an axisymmetric higher-order vortex with  $VN = 6$  exists at  $\Omega = 0.24$ . Axisymmetric vortices with still larger values of  $VN$  appear for  $\Omega \geq 0.24$ , similar to the case of  $\gamma = 0$  shown in Fig. 7.

The results for  $g = 10$  are displayed in Fig. 12. A standing-wave state appears at  $\gamma = 2$  and  $g = 10$ , instead of the plane wave at  $\gamma = 0$  and  $g = 10$ . Actually, this standing wave (at  $g = 10$ ) is similar to the MM state at  $g = 1$ . For larger  $g$ , the wave pattern naturally expands due to the strong self-repulsion, remaining close to the standing wave. Figure 12(a) shows the standing-wave state in component  $\psi_+$  at  $\Omega = 0$ . Figures 12(b) and (c) show wave patterns in the  $\psi_+$  (b) and  $\psi_-$  (c) components at  $\Omega = 0.09$ . The nodal line of the original standing wave is replaced by the vortex array, with the total vorticity corresponding to  $VN = 5$  for  $\psi_+$  and  $VN = 6$  for  $\psi_-$ . As above,  $VN$  of  $\psi_-$  is larger by 1 than  $VN$  of  $\phi_+$ . Figure 12(d) shows the pattern of  $\psi_-$  at  $\Omega = 0.1$ . The single-string vortex array is unstable in this case, being replaced by the trilete pattern.

More complex vortex patterns than the trilete one are observed at larger values of the SOC strength  $\lambda$ . Figure 13 shows the wave patterns for  $\lambda = 5$  (a) and  $\lambda = 8$  (b) with  $g = 10$ ,  $\gamma = 2$ ,  $\Omega = 0.1$ , and  $N = 4$ . Vortex arrays are attached to five and seven domain walls at  $\lambda = 5$  and  $\lambda = 8$ , respectively.

A general conclusion produced by the current analysis is that the pattern's vortex number (topological charge),  $VN$ , increases with the increase of  $\Omega$ . The conclusion is summarized in Fig. 14, which shows the relationship between  $\Omega$  and  $VN$  at  $\gamma = 0$  (a) and  $\gamma = 2$  (b) for  $\lambda = 2$ ,  $g = 10$  and  $N = 4$ . The data plotted in Fig. 14 were collected by the imaginary-time simulations initiated with input given by Eq. (7). The corresponding integer value of  $VN$  was calculated as the sum of topological charges ( $VNs$ ) of the central axisymmetric vortex and unitary vortices forming the arrays. As  $\Omega$  increases, the plane-wave state takes place at  $\Omega \leq 0.04$  if  $\gamma = 0$ . With the increase of  $\Omega$ , the plane wave changes into the straight single-string vortex array, then the trilete one, and, eventually, multi-string arrays.

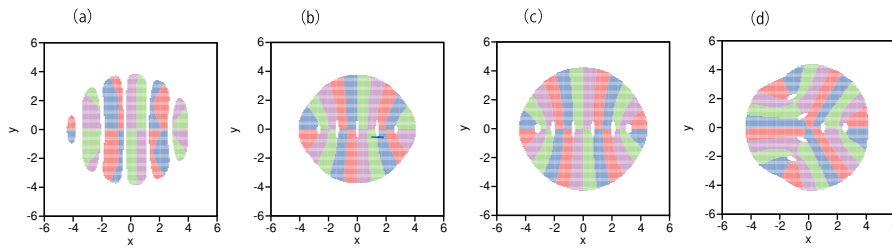


FIG. 12. (a) The standing-wave pattern of component  $\psi_+$  for  $g = 10$ ,  $\gamma = 2$ ,  $\Omega = 0$ ,  $\lambda = 2$ , and  $N = 4$ . Wave patterns of  $\psi_+$  in the region of  $|\psi_+| > 0.08$  are plotted by four colors, as defined in the caption to Fig. 1. (b) The wave pattern of  $\psi_+$  at  $\Omega = 0.09$ . (c) The wave pattern of  $\psi_-$  at  $\Omega = 0.09$ . (d) The wave pattern of  $\psi_-$  at  $\Omega = 0.1$ .

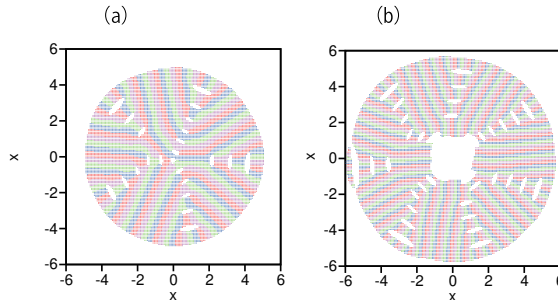


FIG. 13. The wave patterns at  $\lambda = 5$  (a) and  $\lambda = 8$  (b) for  $g = 10$ ,  $\gamma = 2$ ,  $\Omega = 0.1$ , and  $N = 4$ . The arrays of unitary vortices are attached to five and seven domain walls at  $\lambda = 5$  and  $\lambda = 8$ , respectively.

Marks “x” denote intermediate patterns including many unitary vortices. For  $\gamma = 2$ , the standing wave exists at  $\Omega = 0$ . It changes into the straight single-string array at small  $\Omega$ , then the trilete one, and, eventually, multi-string patterns. Marks “\*” denote a pattern formed by unitary vortices attached to four domain walls.

Finally, it is relevant to estimate characteristic parameters of the system in physical units, assuming typical conditions which admit the experimental realization of SOC [33–35]. For the 2D harmonic-oscillator potential (see Eq. (2)) with trapping frequency  $\sim 1$  Hz, SOC spatial scale  $\sim 10 \mu\text{m}$ , transverse trapping size  $\sim 3 \mu\text{m}$ , and the number of atoms in the condensate  $\sim 10^4$ , we conclude that the transitions from the straight (single-string) vortex arrays to the trilete ones, and from the latter ones to the multi-string arrays (see Fig. 14) may take place at the rotation angular velocities  $\Omega \sim 0.1$  Hz and  $0.3$  Hz, respectively.

It is also natural to characterize the sequence of the vortex patterns by the value of their angular momentum (9), defined as per Eq. (9). Accordingly, Fig. 14(c) shows the reduced angular momentum,  $M - \Omega N$ , as a function of the rotation velocity  $\Omega$  at  $\gamma = 0$ ,  $\lambda = 2$ ,  $g = 10$ , and  $N = 4$ , which corresponds to Fig. 14(a). Naturally, the angular momentum is a monotonously growing function of  $\Omega$ .

## V. CONCLUSION

The objective of this work is to develop the systematic numerical analysis of steadily rotating states in the binary BEC under the action of SOC (spin-orbit coupling) in the combination with the attractive or repulsive intrinsic nonlinearity and axisymmetric trapping potential. The nonlinearity includes cross- and self-interaction terms, with relative strength  $\gamma$ . To this end, the corresponding system of the GPEs (Gross-Pitaevskii equations) is transformed into the rotating reference frame. The transformed system includes effective ZS (Zeeman-splitting) terms. The systematic numerical analysis, based on the imaginary-time simulations, demonstrates deformation of the solitons of the SV (semi-vortex) and MM (mixed-mode) types under the action of rotation, in the case of the attractive nonlinearity. In the case of the repulsive interaction, various vortex patterns appear. For the weakly repulsive interaction at  $\gamma = 0$ , the SV state exists at small values of the rotation velocity  $\Omega$ . It is replaced by a vortex state at larger  $\Omega$ , which is further replaced by a higher-order vortex state at even larger  $\Omega$ . For the strongly repulsive interaction, a single-string array appears at relatively small  $\Omega$ , being replaced by a trilete array at larger  $\Omega$ . Eventually, at still larger values of  $\Omega$ , stable star-shaped arrays emerge, composed of five and seven strings. The transitions are explained by the

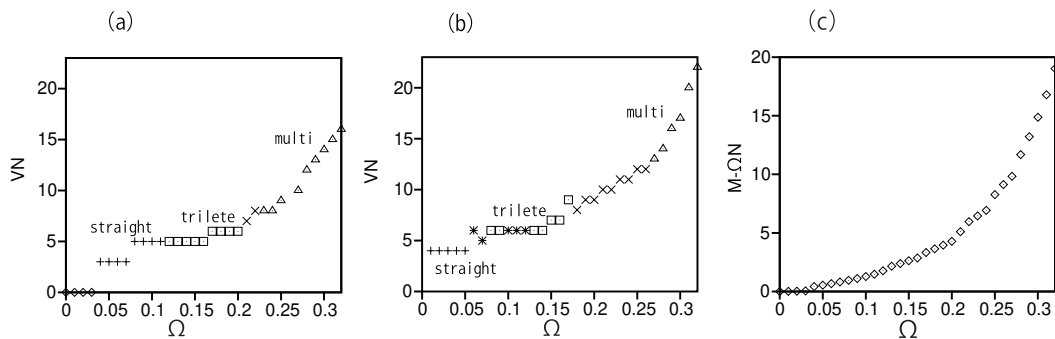


FIG. 14. (a) Vortex number VN as a function of rotation frequency  $\Omega$  for  $\gamma = 0$ ,  $\lambda = 2$ ,  $g = 10$ , and  $N = 4$ . (b) VN vs.  $\Omega$  for  $\gamma = 2$ ,  $\lambda = 2$ ,  $g = 10$ , and  $N = 4$ . (c) The reduced angular momentum  $M - \Omega N$ , defined as per Eq. (9), vs.  $\Omega$  for the same fixed parameters as in panel (a). The results summarized in this figure were produced by means of the imaginary-time evolution method, with the input given by Eq. (7).

comparison of energy of the coexisting patterns of different types. The rectilinear chains of vortices in single- and multi-string patterns are attached to boundaries separating background domains filled by plane waves with different wave vectors. The transition of the axisymmetric higher-order vortex state to the trilete state was studied too, varying the nonlinearity strength  $g$  for fixed values of other parameters. In that case, unitary vortices successively escape from the central higher-order one in three directions, building the trilete pattern.

#### ACKNOWLEDGMENTS

The work of B.A.M. was supported, in a part, by the Israel Science Foundation (grant No. 1695/22).

- 
- [1] J. E. Williams and M. J. Holl, Preparing topological states of a Bose-Einstein condensate, *Nature* **401**, 568 (1999).
  - [2] M. R. Matthews, B. P. Anderson, P. C. Haljan, D. S. Hall, C. E. Wieman, and E. A. Cornell, Vortices in a Bose-Einstein condensate, *Phys. Rev. Lett.* **83**, 2498-2501 (1999).
  - [3] K. W. Madison, F. Chevy, W. Wohlleben, J. Dalibard, Vortex formation in a stirred Bose-Einstein condensate, *Phys. Rev. Lett.* **84**, 806-809 (2000).
  - [4] K. Kasamatsu, M. Tsubota, and M. Ueda, Vortex phase diagram in rotating two-component Bose-Einstein condensates, *Phys. Rev. Lett.* **91**, 150406 (2003).
  - [5] K. E. Strecker, G. B. Partridge, A. G. Truscott, and R. G. Hulet, Formation and propagation of matter-wave soliton trains, *Nature* **417**, 150-153 (2002).
  - [6] L. Khaykovich, F. Schreck, G. Ferrari, T. Bourdel, J. Cubizolles, L. D. Carr, Y. Castin, and C. Salomon, Formation of a matter-wave bright soliton", *Science* **296**, 1290-1293 (2002).
  - [7] S. L. Cornish, S. T. Thompson, and C. E. Wieman, Formation of bright matter-wave solitons during the collapse of attractive Bose-Einstein condensates, *Phys. Rev. Lett.* **96**, 170401 (2006).
  - [8] B. Eiermann, Th. Anker, M. Albiez, M. Taglieber, P. Treutlein, K.-P. Marzlin, and M. K. Oberthaler, Bright Bose-Einstein gap solitons of atoms with repulsive interaction, *Phys. Rev. Lett.* **92**, 230401 (2004).
  - [9] C.-A. Chen and C.-L. Hung, Observation of universal quench dynamics and Townes soliton formation from modulational instability in two-dimensional Bose gases, *Phys. Rev. Lett.* **125**, 250401 (2020).
  - [10] B. Bakkali-Hassani, C. Maury, Y.-Q. Zhou, E. Le Cerf, R. Saint-Jalm, P. C. M. Castilho, S. Nascimbene, J. Dalibard, and J. Beugnon, Realization of a Townes soliton in a two-component planar Bose gas, *Phys. Rev. Lett.* **127**, 023603 (2021).
  - [11] C. Cabrera, L. Tanzi, J. Sanz, B. Naylor, P. Thomas, P. Cheiney, and L. Tarruell, Quantum liquid droplets in a mixture of Bose-Einstein condensates, *Science* **359**, 301-304 (2018).
  - [12] P. Cheiney, C. R. Cabrera, J. Sanz, B. Naylor, L. Tanzi, and L. Tarruell, Bright soliton to quantum droplet transition in a mixture of Bose-Einstein condensates, *Phys. Rev. Lett.* **120**, 135301 (2018).
  - [13] G. Semeghini, G. Ferioli, L. Masi, C. Mazzinghi, L. Wolswijk, F. Minardi, M. Modugno, G. Modugno, M. Inguscio, and M. Fattori, Self-bound quantum droplets of atomic mixtures in free space?, *Phys. Rev. Lett.* **120**, 235301 (2018).
  - [14] C. D'Errico, A. Burchianti, M. Prevedelli, L. Salasnich, F. Ancilotto, M. Modugno, F. Minardi, and C. Fort, Observation of quantum droplets in a heteronuclear bosonic mixture, *Phys. Rev. Research* **1**, 033155 (2019).
  - [15] D. S. Petrov, Quantum mechanical stabilization of a collapsing Bose-Bose mixture, *Phys. Rev. Lett.* **115**, 155302 (2015).

- [16] D. S. Petrov and G. E. Astrakharchik, Ultradilute low-dimensional liquids, *Phys. Rev. Lett.* **117**, 100401 (2016).
- [17] R. Y. Chiao, E. Garmire, and C. H. Townes, Self-trapping of optical beams, *Phys. Rev. Lett.* **13**, 479-482 (1964).
- [18] L. Bergé, Wave collapse in physics: Principles and applications to light and plasma waves, *Phys. Rep.* **303**, 259 (1998).
- [19] G. Fibich, *The nonlinear Schrödinger equation: singular solutions and optical collapse*, Berlin: Heidelberg; 2015.
- [20] B. A. Malomed, *Multidimensional Solitons* (AIP Publishing, Melville, NY, 2022).
- [21] H. Sakaguchi, B. Li, and B. A. Malomed, Creation of two-dimensional composite solitons in spin-orbit-coupled self-attractive Bose-Einstein condensates in free space, *Phys. Rev. E* **89**, 032920 (2014).
- [22] H. Sakaguchi, E. Ya. Sherman, and B. A. Malomed, Vortex solitons in two-dimensional spin-orbit coupled Bose-Einstein condensates: Effects of the Rashba-Dresselhaus coupling and the Zeeman splitting, *Phys. Rev. E* **94**, 032202 (2016).
- [23] H. Sakaguchi and K. Umeda, Solitons and Vortex Lattices in the Gross-Pitaevskii Equation with Spin-Orbit Coupling under Rotation, *J. Phys. Soc. Jpn.* **85**, 064402 (2016).
- [24] Y. Zhang, M. E. Mossman, T. Busch, P. Engels, and C. Zhang, Properties of spin-orbit-coupled Bose-Einstein condensates, *Front. Phys.* **11**, 118103 (2016).
- [25] S. Gautam and S. K. Adhikari, Vortex-bright solitons in a spin-orbit-coupled spin-1 condensate, *Phys. Rev. A* **95**, 013608 (2017).
- [26] G. Chen, Y. Liu, and H. Wang, Mixed-mode solitons in quadrupolar BECs with spin-orbit coupling, *Commun. Nonlinear Sci. Numer. Simul.* **48**, 318 (2017).
- [27] R. Zhong, Z. Chen, C. Huang, Z. Luo, H. Tan, B. A. Malomed, Y. Li, Self-trapping under two-dimensional spin-orbit coupling and spatially growing repulsive nonlinearity, *Front. Phys.* **13**, 130311 (2018).
- [28] H. Sakaguchi and B. A. Malomed, One- and two-dimensional gap solitons in spin-orbit-coupled systems with Zeeman splitting, *Phys. Rev. A* **97**, 013607 (2018).
- [29] Y. Li, X. Zhang, R. Zhong, Z. Luo, B. Liu, C. Huang, W. Pang, and B. A. Malomed, Two-dimensional composite solitons in Bose-Einstein condensates with spatially confined spin-orbit coupling, *Commun. Nonlinear Sci. Numer. Simul.* **73**, 481 (2019).
- [30] X. Chen, Z. Deng, X. Xu, S. Li, Z. Fan, Z. Chen, B. Liu, and Y. Li, Nonlinear modes in spatially confined spin-orbit-coupled Bose-Einstein condensates with repulsive nonlinearity, *Nonlinear Dynamics* **101**, 569 (2020).
- [31] H. Deng, J. Li, Z. Chen, Y. Liu, D. Liu, C. Jiang, C. Kong, and B. A. Malomed, Semi-vortex solitons and their excited states in spin-orbit-coupled binary bosonic condensates, *Phys. Rev. E* **109**, 064201 (2024).
- [32] Y. Zhang, Z. Zhou, B. A. Malomed, and H. Pu, Stable solitons in three dimensional free space without the ground state: Self-trapped Bose-Einstein condensates with spin-orbit coupling, *Phys. Rev. Lett.* **115**, 253902 (2015).
- [33] Y.-J. Lin, K. Jiménez-García, and I. B. Spielman, Spin-orbit-coupled Bose-Einstein condensates, *Nature* **471**, 83-86 (2011).
- [34] B. M. Anderson, G. Juzeliūnas, V. M. Galitski, and I. B. Spielman, Synthetic 3D spin-orbit coupling, *Phys. Rev. Lett.* **108**, 235301 (2012).
- [35] V. Galitski and I. B. Spielman, Spin-orbit coupling in quantum gases, *Nature* **494**, 49-54 (2013).
- [36] S. Sinha, R. Nath, and L. Santos, Trapped two-dimensional condensates with synthetic spin-orbit coupling, *Phys. Rev. Lett.* **107**, 270401 (2011).
- [37] Z. Wu, L. Zhang, W. Sun, X.-T. Xu, B.-Z. Wang, S.-C. Ji, Y. Deng, S. Chen, X.-J. Liu, and J.-W. Pan, Realization of two-dimensional spin-orbit coupling for Bose-Einstein condensates, *Science*, **354**, 83-88 (2016).
- [38] G. Roati, M. Zaccanti, C. D'Errico, J. Catani, M. Modugno, A. Simoni, M. Inguscio, and G. Modugno, <sup>39</sup>K Bose-Einstein condensate with tunable interactions, *Phys. Rev. Lett.* **99**, 010403 (2007).
- [39] S. B. Papp, J. M. Pino and C. E. Wieman, Tunable miscibility in a dual-species Bose-Einstein condensate, *Phys. Rev. Lett.* **101**, 040402 (2008).
- [40] P. Zhang, P. Naidon and M. Ueda, Independent control of scattering lengths in multicomponent quantum gases, *Phys. Rev. Lett.* **103**, 133202 (2009).
- [41] C. Chin, R. Grimm, P. Julienne, and E. Tiesinga, Feshbach resonances in ultracold gases, *Rev. Mod. Phys.* **82**, 1225-1286 (2010).
- [42] X.-Q. Xu and J. H. Han, Spin-orbit coupled Bose-Einstein condensate under rotation, *Phys. Rev. Lett.* **107**, 200401 (2011).
- [43] X.-F. Zhou, J. Zhou, and C. Wu, Vortex structures of rotating spin-orbit-coupled Bose-Einstein condensates, *Phys. Rev. A* **84**, 063624 (2011).
- [44] R. A. Duine and H. T. C. Stoof, Atom-molecule coherence in Bose gases, *Phys. Rep.* **396**, 115-195 (2004).
- [45] Y. V. Kartashov, V. V. Konotop, and F. K. Abdullaev, Gap solitons in a spin-orbit-coupled Bose-Einstein condensate, *Phys. Rev. Lett.* **111**, 060402 (2013).
- [46] M. L. Chiofalo, S. Succi, and M. P. Tosi, Ground state of trapped interacting Bose-Einstein condensates by an explicit imaginary-time algorithm, *Phys. Rev. E* **62**, 7438-7444 (2000).
- [47] W. Z. Bao and Q. Du, Computing the ground state solution of Bose-Einstein condensates by a normalized gradient flow, *SIAM J. Sci. Comp.* **25**, 1674-1697 (2004).
- [48] M. Vakhitov, and A. Kolokolov, Stationary solutions of the wave equation in the medium with nonlinearity saturation, *Radiophys. Quantum Electron.* **16**, 783 (1973).
- [49] H. Sakaguchi and B. A. Malomed. Solitons in combined linear and nonlinear lattice potentials, *Phys. Rev. A* **81**, 013624 (2010).
- [50] W. J. Thompson, *Angular Momentum: An Illustrated Guide to Rotational Symmetries for Physical Systems*, Volume 1 (Wiley-VCH, Hoboken, New Jersey, 1994).